Zhou, Y., Lühr, H. (2017): Net ionospheric currents closing field-aligned currents in the auroral region: CHAMP results. - *Journal of Geophysical Research*, *122*, 4, pp. 4436—4449.

DOI: http://doi.org/10.1002/2016JA023090

AGU PUBLICATIONS

JGR

Journal of Geophysical Research: Space Physics

RESEARCH ARTICLE

10.1002/2016JA023090

Key Points:
- Investigation of net ionospheric currents closing field-aligned currents derived from the integration of magnetic field along CHAMP orbit
- For the first time presentation of full local time and seasonal variation of net current, separately for both hemispheres
- Net duskward and antisunward currents show opposite seasonal dependences. Current intensities vary out of phase between the hemispheres

Correspondence to:
Y.-L. Zhou,
zhouyl@whu.edu.cn

Citation:
Zhou, Y.-L., and H. Lühr (2017), Net ionospheric currents closing field-aligned currents in the auroral region: CHAMP results, *J. Geophys. Res. Space Physics*, *122*, 4436–4449, doi:10.1002/2016JA023090.

Received 20 JUN 2016
Accepted 10 MAR 2017
Accepted article online 15 MAR 2017
Published online 1 APR 2017

Net ionospheric currents closing field-aligned currents in the auroral region: CHAMP results

Yun-Liang Zhou[1,2] and Hermann Lühr[2]

[1]Department of Space Physics, School of Electronic Information, Wuhan University, Wuhan, China, [2]GFZ German Research Centre for Geosciences, Potsdam, Germany

Abstract By utilizing the high-resolution and precise vector magnetic field measurements from CHAMP during 2001–2005, the characteristics of the net auroral currents calculated by Ampère's integral law are comprehensively investigated. It is found that the net currents deduced from noon-midnight (dawn-dusk) orbits are directed duskward (antisunward). The intensities of the net currents increase linearly when the merging electric field (E_m) is growing, exhibiting maximum values of about 2 (1) MA for the net duskward (antisunward) currents when E_m exceeds 4 mV/m. For the first time the seasonal variations of the different net currents are shown. The net currents deduced from full orbits show only little seasonal dependence due to a compensation of the effects between the hemispheres. Conversely, the net currents deduced separately for the two hemispheres exhibit prominent seasonal dependences. For the net duskward currents the amplitudes and slopes of E_m dependence are both larger by a factor of about 2 in summer than in winter. The related cross-polar cap Pedersen currents are higher in the sunlit hemisphere due to enhanced conductivity. The summer-time duskward currents are larger in the Northern Hemisphere than in the Southern Hemisphere by a factor of 1.5. Conversely, the net antisunward currents show an opposite seasonal dependence. The ratio of summer to winter intensity amounts to about 0.7. In this case the currents are stronger in the Southern Hemisphere.

1. Introduction

Satellite missions offer the opportunity to deduce the net electric current flowing through the orbital loop. *Suzuki and Fukushima* [1982] were the first to apply Ampère's integral law to the along-track magnetic field component from the Magsat. In a follow-on study *Suzuki et al.* [1985] provided a clear evidence for antisunward current amounting to more than one million Ampère (MA) during times of large magnetic activity. Due to Magsat's Sun-synchronous dawn-dusk orbit no other current components could be investigated. About 20 years later the Ørsted mission allowed investigating net auroral currents in other directions. By considering 5 months of magnetic field measurements from orbits around the noon-midnight meridian *Stauning and Primdahl* [2000] could determine net dawn-to-dusk currents. They clearly showed that the intensity of the duskward electric currents, which to first order represent the closure of excessive Region 1 (R1) field-aligned currents (FACs) that are not closed by R2 FACs, depends on two parameters. Most important is the driving by the "geo-effective" solar wind electric field, also termed "merging electric field (E_m)." The other factor is the solar zenith angle, which directly controls the conductivity of the ionosphere in the polar cap area. Also, in the case of dawn-to-dusk current, intensities of more than 1 MA have been observed during times of enhanced solar wind input.

As mentioned before, several earlier studies attempted to quantify the net auroral currents and their drivers. However, due to the life spans and orbit features of Magsat and Ørsted missions, it is not easy to compile a comprehensive picture of the large-scale geospace electrical currents from the previous results. The remaining questions are as follows: What are the seasonal variations of the current components, what are the parameters determining their intensity, and how are the net currents closed?

Thanks to the CHAMP satellite with its high-inclination orbit, long-term mission, and good data coverage, several of these questions can be addressed. In this study we will make use of the high-resolution and precise magnetic field measurements from the Fluxgate Magnetometer (FGM) onboard CHAMP during the active 5 years (2001–2005). By applying Ampère's integral law we systematically investigate the characteristics of the net auroral currents, both the duskward and antisunward current components. For further detailing the auroral current variations with season, local time, and solar wind input we investigate the

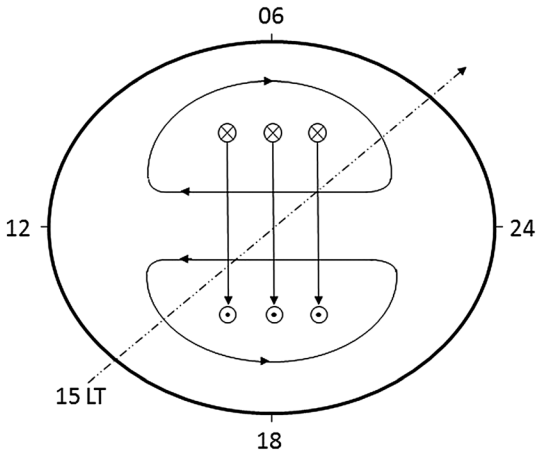

Figure 1. Schematic illustration of the auroral current system in local time frame. An example orbit of CHAMP with orbit local time of 15 LT is indicated by the dashed line.

net currents individually for the two hemispheres. The ultimate aim of the study is to improve our understanding of the complete auroral current circuit and the magnetosphere-ionosphere coupling processes.

In the following section general features of the auroral current system are described and the determination approach of net current enclosed by CHAMP orbits at different local time is introduced. Subsequently, we outline the data set and the processing strategies. The observed results of our statistical analysis are presented in section 4. In section 5 the findings are discussed and compared with previous publications. Finally, we summarize our main results.

2. Auroral Current System and the Net Currents Enclosed by CHAMP Orbits

It is generally accepted that the auroral current system comprises FACs, Pedersen currents, and Hall currents, and all these currents are tightly related to each other at high-latitude regions. The FACs flow into and out of the ionosphere at auroral latitudes, and they contribute significantly to the coupling between the ionosphere and magnetosphere. Their average distribution in latitude and local time has first been presented by *Iijima and Potemra* [1976] and in principle is still valid today. Pedersen currents are horizontal currents flowing in the direction of the electric field, which primarily perform the ionospheric current closure between FACs. Hall currents flow transverse to the electric and magnetic fields, encircling FAC sheets. To first order they are source-free and flow in opposite direction to the $E \times B$ plasma drift. A good description of all these currents can be found, for example, in the review article of *Cowley* [2000]. Figure 1 shows schematically the distribution of major auroral currents in a local time (LT) frame. For FACs we show only the R1 currents. One can see that on the duskside (dawnside) the R1 FACs flow out of (into) the ionosphere at the high-latitude boundary of the auroral oval. Over the polar cap region part of the R1 FAC is diverted into Pedersen currents flowing from dawnside to duskside. Hall currents, flowing antisunward on the duskside and dawnside at auroral latitudes, are commonly termed auroral electrojets. The return currents are expected to flow over the polar cap for closing the circuit, at least in case of a sufficient ionospheric conductivity.

The CHAMP satellite on its near polar and circular orbit samples the magnetic field on a closed circle, almost fixed in local time, for each orbit. By applying Ampère's integral law to the along-track component of the magnetic field, the net currents enclosed by the circle can be derived. As indicated in Figure 1, the dashed line denotes an example of CHAMP orbit for which the orbit local time is 15 LT. In this study the orbit LT reflects the local time of the satellite when crossing the equator on the upleg pass. For CHAMP it takes 260 days to cover all 24 h of local time. During that time period the auroral current system is crossed along the same profile twice, once on upleg and once on downleg passes. Our ring integration returns the net current flowing transverse to the orbital plane. By that we can study the different current components separately. For example, the net dawnward/duskward current can be deduced from noon-midnight orbits, and the net sunward/antisunward current from dawn-dusk orbits.

3. Data Set and Processing Approach

3.1. Data Set

3.1.1. CHAMP Mission and FGM Data

The CHAMP mission, mainly devoted to global investigations of the gravity field, magnetic field, and to atmospheric profiling, was launched into a near-circular polar orbit (inclination of 87.3°) with an initial altitude of

456 km on 15 July 2000 [*Reigber et al.*, 2002]. By the end of the mission, 19 September 2010, the orbit had decayed to 250 km. The orbital plane covers all local times within 130 days when considering upleg and downleg arcs. The Fluxgate Magnetometer (FGM) onboard CHAMP recorded the vector magnetic field every 0.02 s with a resolution of 0.1 nT. The FGM magnetic field readings are calibrated routinely by using the observations of the onboard absolute scalar Overhauser Magnetometer as a reference. In this study the fully calibrated Level-3 magnetic field products (product identifier: CH-ME-3-MAG) are used, which is provided in the North-East-Center (NEC) frame with a time resolution of 1 Hz. The time period considered comprises the 5 years from 2001 to 2005, experiencing solar activity from high to moderate levels. The 5 years of high-resolution and precise vector magnetic field observations provide an even local time coverage during all seasons.

3.1.2. Solar Wind and Interplanetary Magnetic Field Data

For the description of the conditions in the solar wind the 1 min interplanetary magnetic field (IMF) and solar wind data are downloaded from the OMNI database (available at ftp://spdf.gsfc.nasa.gov/pub/data/omni/high_res_omni/). The data have been propagated to the Earth's bow shock from original observations by multiple spacecraft as ACE, Wind, Geotail, and so on. We use the OMNI data to calculate the merging electric field (E_m), which is taken as a measure for the solar wind input.

3.2. Processing Approach

3.2.1. Ampère's Integral Law

For calculating the net current flowing through the closed satellite orbit, we have applied Ampère's integral law to the along-track magnetic field observations in the form

$$I = \frac{1}{\mu_0} \oint_L B_{\mathrm{AT}}\, dl \tag{1}$$

where μ_0 is the permeability of free space; L is the closed contour, which is taken to be the CHAMP orbit; dl is a differential path element along the CHAMP orbit; B_{AT} is the along-track magnetic field component caused by the current; and I is the net current flowing through the satellite orbital plane encircled by the contour L. Equation (1) can be written in discrete form as

$$I = \frac{1}{\mu_0} \sum_{m=1}^{n} B_{\mathrm{AT}m} \cdot \Delta l \tag{2}$$

where m is the summing index, n is the number of B_{AT} values used to calculate I in a closed contour, and Δl is the path length per increment (here 7.56 km for 1 s). For the circular orbit of CHAMP, as in this study, equation (2) can be written as

$$I = \frac{2\pi r}{\mu_0 n} \sum_{m=1}^{n} B_{\mathrm{AT}m} \tag{3}$$

where r is the radius of the circular orbit. Here we use equation (3) to calculate the net current from full orbits.

3.2.2. Determination of the Along-Track Magnetic Field Component

Our current calculations are based on the along-track magnetic field readings caused by ionospheric currents. For obtaining the ionospheric current effects we first remove the main, crustal, and magnetospheric fields by subtracting the POMME-6 model [*Maus et al.*, 2010; *Lühr and Maus*, 2010] from the actual magnetic field measurements of CHAMP. The residuals are labeled B_l. In a next step the residuals B_l, given in North-East-Center (NEC) frame, have to be rotated into the along-track flight direction, which can be written as

$$B_{\mathrm{AT}} = B_{xl} \cos\gamma + B_{yl} \sin\gamma \tag{4}$$

where B_{AT} is the along-track component, B_{xl} is the northward component, and B_{yl} is the eastward component in NEC frame; the rotation angle γ can be calculated as $\gamma = \arcsin[\cos(\mathrm{incl})/\cos\beta]$ for upleg and $\gamma = \pi - \arcsin[\cos(\mathrm{incl})/\cos\beta]$ for downleg arcs; incl is the inclination of the orbit (87.3° for CHAMP); and β is the latitude of satellite position. By applying B_{AT} to equation (3) the net ionospheric current enclosed by the CHAMP orbit can be derived.

Figure 2 shows an example of B_{AT} for 22 August 2001 (from 14:19 to 14:38 UT). During this period of time moderate magnetic activity prevailed ($Kp = 4$). For completeness the corresponding magnetic latitude

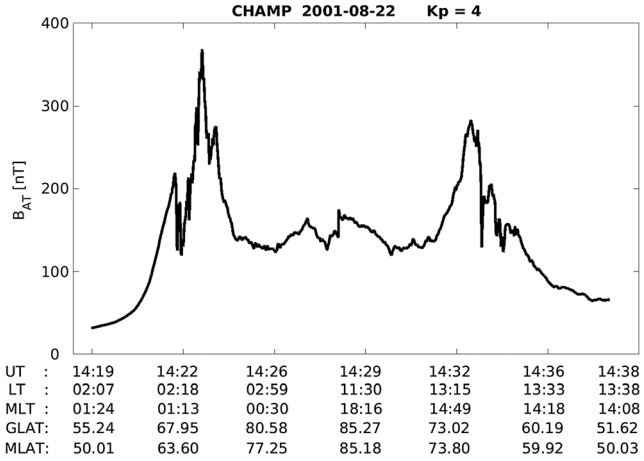

Figure 2. An example of the along-track magnetic field residuals from CHAMP for a pass over the northern polar region.

(MLAT), geographic latitude (GLAT), magnetic local time (MLT), and LT are listed at the bottom of the panel. It can be seen that the values of B_{AT} become larger over the auroral region, with maximum values close to 370 nT. Beyond the auroral oval B_{AT} is much smaller, particularly at the equatorward boundary on the nightside. The large values of B_{AT} at high latitudes can be attributed to the auroral currents.

3.2.3. Estimation of Solar Wind Input

It is generally accepted that the auroral currents are predominantly driven by solar wind input. We thus need a suitable coupling function between the solar wind and magnetosphere-ionosphere system. In this study we will utilize the coupling function as defined by *Newell et al.* [2007]. In order to make it comparable with the solar wind electric field, we have somewhat rescaled the value and termed the quantity merging electric field, E_m

$$E_m = \frac{1}{3000} V_{SW}^{\frac{4}{3}} \left(\sqrt{B_y^2 + B_z^2}\right)^{\frac{2}{3}} \sin^{\frac{8}{3}}\left(\frac{\theta}{2}\right) \tag{5}$$

where V_{SW} is the solar wind velocity in km/s, B_y and B_z both in nT are the IMF components in GSM coordinates, and θ is the clock angle of the IMF. With these units the value of the merging electric field will result in mV/m. Due to the propagation time from the bow shock to the ionosphere we have considered a delay of 20 min and smoothed the E_m values over 15 min. This kind of conditioning has been found to be suitable for ionospheric studies like *Kervalishvili and Lühr* [2014, and references therein].

4. Statistical Results

As mentioned before, the data utilized span the time interval from 1 January 2001 to 31 December 2005. During this period of time 24,440 out of 28,338 CHAMP orbits are selected for this investigation. Those orbits, in which the data gaps exceed 100 s at low and middle latitudes (GLAT $< 60°$) and 20 s at high latitudes (GLAT $\geq 60°$), are discarded. The smaller data gaps are interpolated by linear (low and middle latitudes) or spline interpolation (high latitudes). The large number of orbits provides a good basis for statistical analyses, allowing us to sort the observations according to different conditions and study various aspects.

4.1. Full Orbit Net Current Estimates

By applying Ampère's integral law to B_{AT} the net current can be obtained from each orbit. For studying the characteristics, we first sorted the derived net currents into four activity groups based on E_m values in units of mV/m ($0 < E_m \leq 1$, $1 < E_m \leq 2$, $2 < E_m \leq 4$, and $E_m > 4$). For each group the results were binned into grids of month of year (1 month) by orbit LT (1 h). Here the orbit LT denotes the local time when CHAMP crosses the equator on upleg pass. Current results are sorted into 24 overlapping bins of 2 h width spaced by 1 h in local time. Figure 3 shows the net current distributions in an orbit LT versus month frame for the different levels of E_m intensity. The blank areas in Figure 3d are due to lack of data. It has to be noted that the range of the color bars is different for the top and bottom plots. For the interpretation it should be kept in mind that currents derived from midnight orbits flow in duskward direction, and dawn orbits (06 LT) reflect antisunward currents. From Figure 3 we can see that we obtain positive (negative) values for the midnight (noon) orbits indicating duskward currents; similarly, the positive (negative) values for dawn (dusk) orbits denote antisunward currents. Furthermore, the amplitudes and directions of net currents vary with orbit local time, E_m level and season. Considering, as an example, the condition for E_m less than 1 mV/m (see Figure 3a), it can be seen that the net currents deduced from the noon and midnight orbits are both directed duskward, and both the

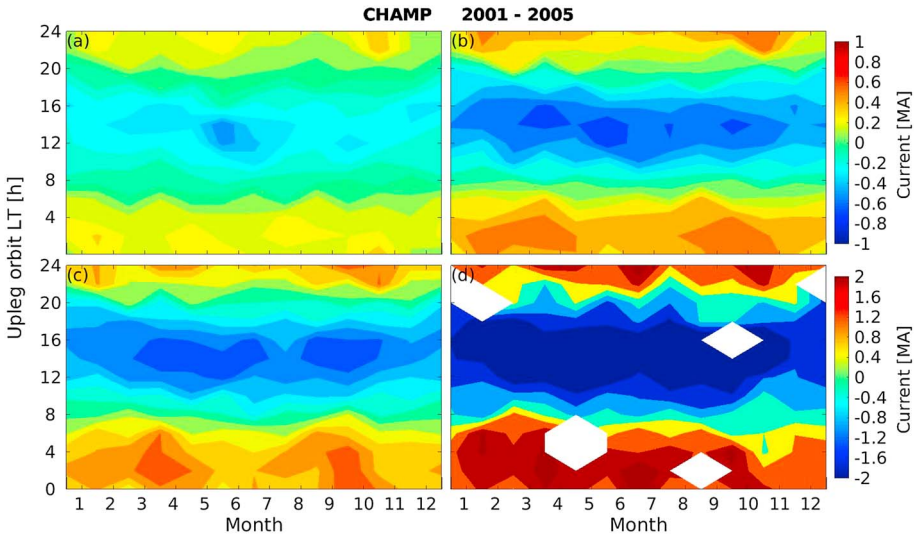

Figure 3. Orbit local time versus month distributions of net currents deduced from full CHAMP orbits for different level of solar wind input, E_m in mV/m: (a) $0 < E_m \leq 1$, (b) $1 < E_m \leq 2$, (c) $2 < E_m \leq 4$, and (d) $E_m > 4$.

dawn and dusk orbits provide antisunward currents. The amplitudes of the net duskward currents are larger than those of the antisunward currents. For the E_m dependence one can see that the amplitudes of the net currents are stronger for larger E_m values, showing maximum net duskward (antisunward) currents approaching 2 (1) MA when E_m values exceed 4 mV/m. This indicates that the enhanced solar wind input leads to stronger net ionospheric currents. In spite of the different magnitudes for different E_m levels, the orbit LT versus month distribution patterns of the net currents are similar. For E_m less than 1 mV/m the duskward currents from noon orbits show maximum values around June solstice. Except for this feature the net ionospheric currents exhibit no prominent seasonal dependence during low activity. However, when E_m values vary between 1 and 4 mV/m (see Figures 3b and 3c), it seems that the net ionospheric currents exhibit larger values during equinox seasons. We will revisit this topic in section 5.2.

For depicting the average local time variation of derived net currents, Figure 4 shows two curves, one for June and the other for December solstice months. The orbit LT variations of the net currents for these two seasons are quite similar. Expected hemispheric differences seem to compensate, but there remains a somewhat larger intensity of net currents around June solstice than December solstice, in particular from orbits around noon. An explanation for this will be offered in the next section.

4.2. Hemispheric Net Current Estimates

For investigating the seasonal and hemispheric characteristics, it is more appropriate to consider the net currents derived from high-latitude passes for the Northern and Southern Hemispheres separately. The auroral current systems in the two hemispheres can be considered as independent, just driven by the same solar wind input. The integration approach applied for single hemisphere is depicted schematically in Figure 5. For each orbit we consider the high-latitude magnetic field measurements from a given hemisphere over the MLAT range exceeding 50° (path A→B). The virtual integration path continues vertically downward to the Earth surface (B–C), along the Earth surface (C–D) and vertically up again (D–A) to the starting point of the closed contour. We may assume that the contributions of B_{AT} to the ring integral are relatively small from the dashed part of the virtual path. The net currents we analyze are connected to FACs at their ends. According to Fukushima's theorem [*Fukushima*, 1976] the magnetic effect of a pair of antiparallel FACs connected by horizontal currents in the ionosphere will disappear on ground. The current configuration in our case, however, differs somewhat from the ideal case presented by *Fukushima* [1976], and the theorem might thus not be applicable here.

The chosen approach for estimating the contribution of the unsampled part to the full integration loop (B → C → D → A) is based solely on observations. Our main argument is that the sum of the two hemispheric net currents should be equal to the full-orbit results. The latter do not depend on any assumptions. Our two

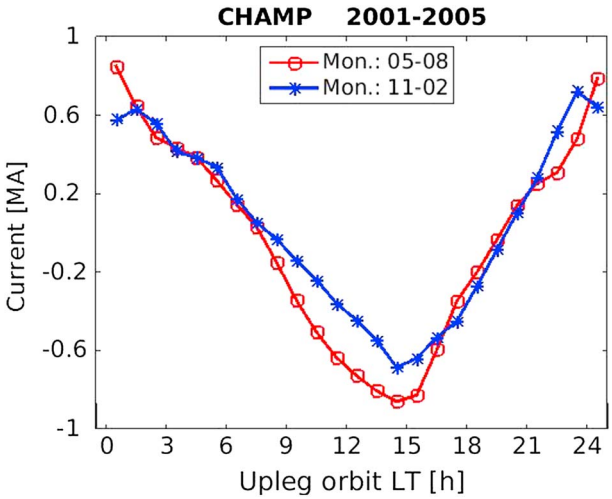

Figure 4. Local time variation of net current intensity deduced from CHAMP full orbits for June (red) and December (blue) solstices.

assumptions are as follows: (1) The contribution from C → D is similar in shape to that from A → B. (2) The contributions from B → C and D → A are proportional to the vertical component B_z at the points A and B since the radial magnetic field varies only smoothly through the current sheet. With these constrains there is only one solution that makes the sum of hemispheric results fitting the full-orbit net currents in both amplitude and phase. An outcome of this exercise is that the integral over A → B has to be multiplied by 1.2 for including the contributions from path C → D and that the vertical magnetic field component, B_{zI}, has to be multiplied by 11 times the orbital altitude and divided by the permeability of free space to represent the contributions from parts (B → C and D → A). These latter contributions add only a few percent to the final value. Their size is depending somewhat on local time. No other combination of scaling factors results in smaller residuals. A more detailed assessment of the incomplete integration loop will be given in section 5.1.

For presenting the results we sort the hemispheric net currents regardless of E_m conditions into grids of month of year (1 month) by orbit MLT (1 h). Here the orbit MLT denotes the magnetic local time when CHAMP crosses 70° MLAT on upleg pass. Figure 6 shows the average net current distribution separately for the Northern and Southern Hemispheres.

Similar to the full-orbit results, the hemispheric net currents derived from the high-latitude passes exhibit on average larger amplitudes for the net duskward currents than for the antisunward currents in both hemispheres. The net duskward currents are larger in the Northern Hemisphere than in the Southern

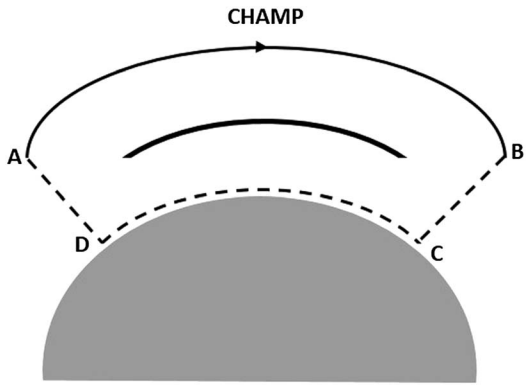

Figure 5. Schematic drawing of the net current determination approach for a single hemisphere. The virtual return path running along the Earth's surface is shown as dashed line.

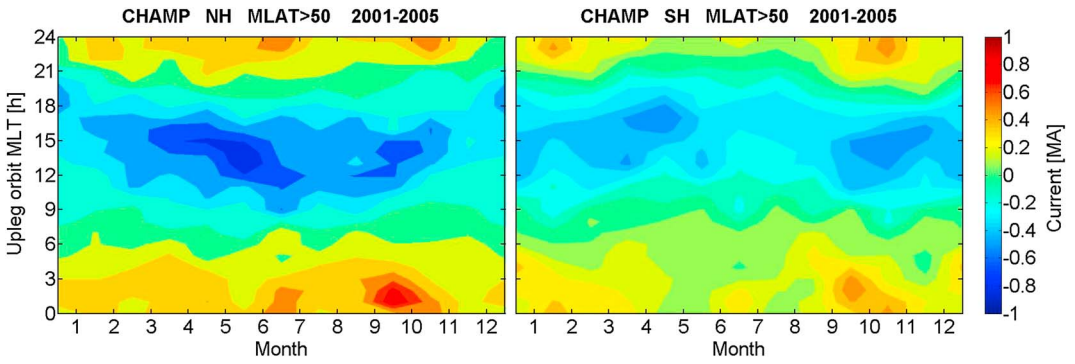

Figure 6. The orbit MLT versus month distributions of net currents derived from high-latitude passes over the (left) Northern and (right) Southern Hemispheres.

Hemisphere, reaching maximum values of about 0.8 MA. Different from the full orbit, the net hemispheric currents show clear seasonal dependences in both hemispheres. For example, the negative currents (blue band in Figure 6) maximize during June solstice around 12 MLT in the Northern Hemisphere and around 18 MLT in the Southern Hemisphere. The opposite relation holds during December solstice exhibiting peak values around 18 MLT in the Northern Hemisphere and around 13 MLT in the Southern Hemisphere. This indicates largest net duskward currents during local summer and largest net antisunward currents during local winter.

In the following a more detailed analysis of the seasonal dependence of the net duskward and antisunward currents is performed. For improving the statistic we combine the net duskward current from observations sampled in the noon and midnight sectors (11–13 MLT and 23–01 MLT). And for the net antisunward currents we combine the observations from the dawn and dusk sectors (05–07 MLT and 17–19 MLT). The seasonal variations of the hemispheric net duskward and antisunward currents are presented in Figure 7. In order

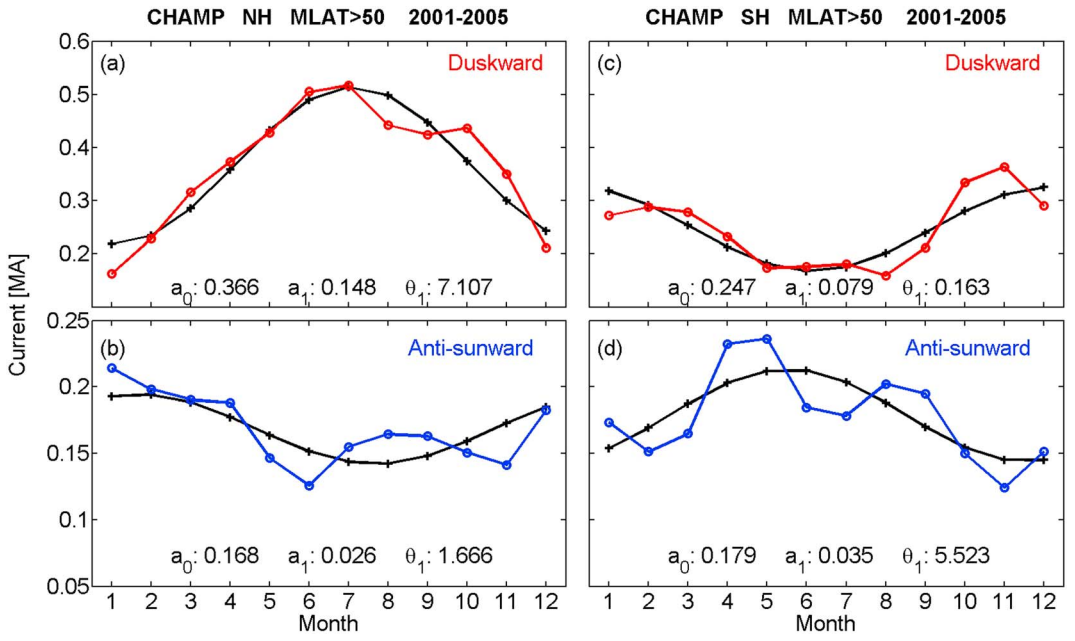

Figure 7. The seasonal variation of net (a and c) duskward and (b and d) antisunward currents derived from high-latitude passes over the Northern (Figures 7a and 7b) and Southern (Figures 7c and 7d) Hemispheres. The observed net duskward currents are shown by red curves, and the blue curves represent antisunward currents. The black curves are sinusoidal fits to the observations. Fitted amplitudes (in MA) for the constant and annual terms, as well as the phases (in month) for the annual terms, are listed in each panel.

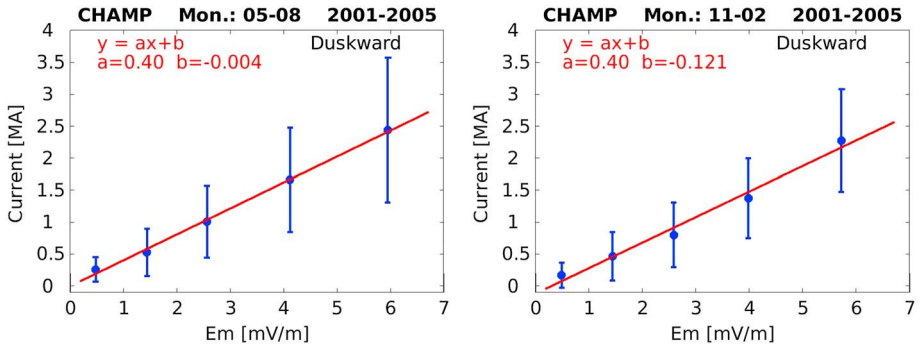

Figure 8. The E_m dependence of net duskward currents derived from full orbits during (left) June and (right) December solstices. The solid dots with vertical bars indicate the mean values and standard deviation of the net duskward current for five levels of E_m, and the lines represent the linear fit to the results. Parameters of the linear fits are listed in the top left corner of each frame.

to better quantify the information about the seasonal dependence of these currents we fit a harmonic function to the data

$$I_{\text{fit}} = a_0 + a_1 \cdot \cos[\omega(t - \theta_1)] \tag{6}$$

where I_{fit} is the current derived from a fit to observations, $\omega = \frac{2\pi}{12}$ is the frequency per year, t denotes the time in month of a year, θ_1 is the phase (in units of month) of the annual term and reflects the month of peak current, and a_0 and a_1 are the amplitudes (in units of MA) of the constant and annual terms, respectively. In Figure 7 the obtained results are listed in each panel.

In the Northern Hemisphere the net duskward current exhibits a prominent seasonal variation, with largest amplitude in local summer (peak value middle of July). The average amplitudes during local summer and winter amount to 0.51 MA and 0.22 MA, respectively, giving an amplitude ratio of 2.3, while the net antisunward current has an opposite seasonal dependence, showing smaller amplitude in local summer (0.14 MA) than in local winter (0.19 MA) resulting in a ratio of 0.73. In the Southern Hemisphere the observed net duskward current is consistent with the seasonal dependence of the Northern Hemisphere, and exhibiting an amplitude ratio between local summer and winter of about 1.9. Also, the net antisunward currents are smaller in local summer than in winter by a ratio of 0.67, similar to the Northern Hemisphere. With respect to the interhemispheric differences, the mean duskward current intensity is larger in the Northern Hemisphere by a factor of 1.5 than in the Southern Hemisphere. However, the mean antisunward current is larger in the Southern Hemisphere by 7% than in the Northern Hemisphere. Similarly, as for the full orbit results, the hemispheric net duskward currents are larger than the net antisunward currents in both hemispheres. Besides the harmonic seasonal variation the antisunward currents show local peaks around equinoxes (see Figure 7). We relate these to the Russell-McPherron effect [*Russell and McPherron*, 1973].

4.3. Dependence on Solar Wind Input and Solar Flux

We have also investigated how the net currents, deduced from both the full orbits and the individual hemispheres, respond to solar wind input. As mentioned before, the E_m is used as a measure for the solar wind input. For determining the dependence of net currents on E_m our database is divided into five levels of prevailing E_m values (in units of mV/m): $0 < E_m \leq 1$, $1 < E_m \leq 2$, $2 < E_m \leq 3.5$, $3.5 < E_m \leq 5$, and $5 < E_m \leq 7$. For each of the activity classes the average value of E_m and the mean value of the net current, as well as standard deviation, are calculated, separately for duskward and antisunward currents and for the two solstice seasons. Outliers deviating from the mean value by more than 2 times of the standard deviation are discarded.

As an example, the dependence of net duskward currents from full orbits on E_m is shown in Figure 8. Duskward currents are derived from observations taken at 12–14 LT orbits and 00–02 LT orbits. The results are presented separately for June and December solstices. For June solstice we have considered the months from May to August and for December solstice the months from November to February. The solid dots with vertical bars denote the mean values and standard deviations of the net duskward current at the five levels of E_m. A linear regression line is fitted to the mean values. The results of linear regression are shown at the top left corner, where a is the slope (in units of 10^9A m/V) and b is the intercept (in units of MA). It can be seen that

Table 1. The E_m Dependence of the Net Duskward and Antisunward Currents During June and December Solstices

		Full Orbit		Northern Hemisphere		Southern Hemisphere	
Season	Current Direction	Slope (10^9 Am/V)	Inter. (MA)	Slope (10^9 Am/V)	Inter. (MA)	Slope (10^9 Am/V)	Inter. (MA)
Month: 05–08	Duskward	0.40	−0.004	0.34	−0.08	0.11	−0.06
	Antisunward	0.28	−0.228	0.14	−0.11	0.22	−0.15
Month: 11–02	Duskward	0.40	−0.121	0.17	−0.08	0.24	−0.09
	Antisunward	0.30	−0.164	0.19	−0.10	0.07	0.03

a good linear relation between the duskward current intensity and the merging electric field is obtained. There is no sign of saturation for high solar wind input. Interestingly, the slopes obtained for the two solstice seasons are the same, indicating that seasonal effects are compensated between the hemispheres. From the small intercepts we can conclude that the net duskward currents vanish when E_m approaches zero. This infers that the R1 and R2 FACs are well balanced during quiet times, and there is no need for a cross-polar cap net current. Quite similar results have been obtained for the antisunward currents. Also, in that case a linear dependence on E_m emerges, and values approach zero for vanishing E_m. Numerical results for the dependences on the merging electric field are listed in Table 1.

In addition, we also studied the E_m dependence of the hemispheric net duskward and antisunward currents derived from high-latitude passes over the two hemispheres. Using the aforementioned approach, the relations of these hemispheric net currents with E_m for different seasons are obtained. The slopes and intercepts between the hemispheric net currents and E_m derived from linear fits for different conditions are also listed in Table 1. It can be seen that all the slopes are positive confirming stronger net currents when the solar wind input increases. Again, the intercepts are small in all cases indicating vanishing ionospheric net currents during quiet periods. In the Northern Hemisphere the slopes between the hemispheric net duskward current and E_m are 0.34 and 0.17 for local summer and winter, respectively. The ratio of slopes between local summer and winter is 2.0. In the Southern Hemisphere the slopes for the local summer and winter are 0.24 and 0.11, resulting in a ratio of 2.2. This indicates that the conductance in both hemispheres is about 2 times larger in local summer than in local winter. While for the hemispheric antisunward current the E_m dependence has different characteristics for different seasons. From Table 1 it can be seen that in the Northern Hemisphere the slopes for local summer and winter are 0.14 and 0.19, respectively, resulting in a ratio of the slopes between local summer and local winter of 0.73, whereas we get a larger contrast of 0.32 in the Southern Hemisphere. For this current component spatial gradients of conductance are mainly important, as will be discussed in the next section.

Similar to the E_m dependence we have also attempted to analyze the dependence of the net currents on solar flux. Here we limited our attention to small E_m values, below 1 mV/m, in order to avoid a contamination of the solar flux effect by the solar wind input. The distribution of net currents versus the $F_{10.7}$ index shows a lot of scatter, but no significant dependence on solar flux level could be found (figure not shown). This may be surprising since $F_{10.7}$ values varied during the years (2001–2005) between 80 and 220 solar flux unit. In any case, the dependence of net auroral current on solar flux level must be small.

5. Discussion

5.1. Validity of Results

For the application of Ampère's integral law it is required that the integration is performed along a closed path. After removal of the main field contribution this is well satisfied by the CHAMP orbit, since it drifts only 0.35 min in local time each orbit. There is another condition related to Ampère's integral law, namely, the stationarity of currents over the time of sampling. This requirement is difficult to satisfy, when considering the full-orbit results since one revolution takes about 93 min. For investigating the two hemispheric net currents separately, we apply Ampère's integral only to the high-latitude regions and close the loop via a virtual path running along the Earth's surface. Our second method comes closer to satisfying the second requirement because it takes less than 20 min for sampling the high-latitude region. A possible caveat of the second method is that we have to estimate the magnetic field signatures along the return path. For obtaining a first-order estimate of expected magnetic effects along the unsampled parts of the integration

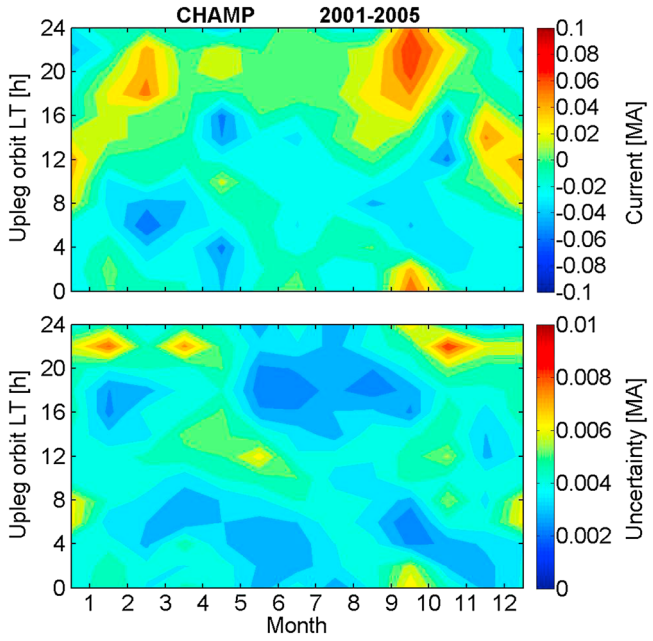

Figure 9. (top) Difference between the sum of hemispheric net currents and the full-orbit results. (bottom) Uncertainty of the bin averages presented above.

path we have evaluated a simple current model. The synthetic current system consists of downward FACs at noon and upward FACs at midnight. Antisunward currents along 70° latitude arcs on the morning and evening sides connect the FACs at ionospheric heights. Magnetic fields are calculated along a dawn/dusk path, as shown in Figure 5. For validation we integrated the along-track magnetic field component according to equation (2) and can confirm that Ampère's law returns the inserted net current of 1 MA. Of interest for our study is the partitioning of contributions from the different arcs along the contour. About 80% of the signal for the current comes from orbital arc at 400 km altitude, 18.3% from the ground arc, and the remaining 1.7% from the two vertical parts. Interestingly, the magnetic signatures at satellite altitude and at the surface look quite similar. It is mainly the bias caused by the magnetic field of the FACs that makes the difference in the contributions from ground track and orbit to the integral. These results provide a lot of support for our corrections of the hemispheric current estimates, as described in section 4.2. The upscaling of the measurements from the orbit arc (A → B) by a factor of 1.2 is well confirmed by our model. Our rescaling of CHAMP measurements corrects in practice also for any small contribution from subsurface induction currents. The contribution from the vertical side parts is in our applied approach somewhat larger than the 1.7%, as predicted by the model. This can be explained by the simple current configuration evaluated. Besides the agreement with the model, for us more important is the confirmation of our hemispheric currents by the full-orbit results. Figure 9 (top) shows the difference between the sum of hemispheric net currents and the full-orbit results. In most places the difference is below 40 kA. There appears no systematic dependence of the residuals on local time or on season. For that reason we consider the seasonal variation in Figure 7 as reliable. In the residuals we find some peaks, in particular around October, reaching 100 kA. Those can be related to big storms. For further demonstrating the reliability of the differences presented in Figure 9 (top), we show in the lower frame the uncertainties (standard deviation divided by square root of sample number) of the individual bin averages. Overall, the values are very small. All this implies that the mean uncertainty of the hemispheric net currents, when distributing the differences (Figure 9, top) evenly between the two hemispheres, amounts to only some tens of kiloampere.

Thanks to the large number (24,440) of orbits considered, any effect of current variability during the time period of integration will average out and does not affect much the mean value. In this same way the reliability of the net current dependence on season and solar wind input gains from the large sample number. Even though the spread of individual values is quite large, as evident from the standard deviation in Figure 8, the uncertainty of derived mean values is low. The uncertainty of a mean value is derived by dividing the standard deviation by the square root of independent net current observations contributing to a group of E_m level. Due to the large number of samples the resulting linear slopes are uncertain only by a few percent.

5.2. Net Duskward Current

As illustrated in Figure 1, the net ionospheric duskward current, crossing the polar cap, connects the excessive R1 FACs on the dawnside and duskside. It can be deduced from the satellite passes on noon-midnight

orbits. Our results show that this net current is on average always duskward, as determined both for the full orbit and the individual high-latitude passes, which is consistent with the results from Ørsted [*Stauning and Primdahl*, 2000]. The net duskward current derived from full orbits reaches values of about 1 MA for E_m in the range from 2 to 3 mV/m (see Figure 8), which is comparable with the result reported by *Stauning and Primdahl* [2000] when the solar illumination is high (see their Figure 3).

As a consequence of enhanced solar wind input into the magnetosphere-ionosphere system, the high-latitude currents and electric fields become stronger. Our results confirm that the net duskward current increases linearly as E_m enhances (see Figures 3 and 8), which is consistent with the results reported by *Christiansen et al.* [2002], who found that the imbalance in current strength between R1 and R2 FACs becomes stronger during disturbed conditions.

The net current derived from full orbits near noon-midnight exhibits larger values during equinoxes for E_m values from 1 to 4 mV/m (see Figures 3b and 3c). This may be related to the Russell-McPherron effect [*Russell and McPherron*, 1973]. During equinoxes more events may populate the top ranges of the activity classes. But we have no conclusive explanation for the mechanism making the R1 FACs stronger for a given E_m value during equinoxes. Except for these maxima at equinoxes no clear seasonal dependence can be detected in Figures 3 and 4. This is also confirmed by the ratio between the net duskward current and the merging electric field, which amounts to 0.4×10^9 A m/V for both June and December solstices (see Figure 8). This suggests that seasonal effects on conductance compensate each other quite well in the two hemispheres.

When treating the two hemispheres separately somewhat different results are obtained. The seasonal dependences are prominent in the duskward currents at the two hemispheres (see Figures 6, 7a, and 7c). The net duskward currents in both hemispheres exhibit 2 times larger value in local summer than in winter. This is clearly related to the amount of solar insolation. But the currents do not go to zero during the dark winter months. From Table 1 it can be seen that also the scaling factor for the dependence on E_m differs between local summer and winter by about 2, 2.0 (2.2) in the Northern (Southern) Hemisphere. Our results on the seasonal dependence of the cross-polar cap duskward current are well consistent with previous findings from field-aligned currents. It is reported that the Northern Hemisphere FAC intensities on the dayside are larger by a factor of about 2 during the summer than winter [*Fujii et al.*, 1981]. Based on Magsat and Ørsted magnetic field observations *Christiansen et al.* [2002] reported that FAC intensities are larger by a factor of 1.5–1.8 in the summer dayside sunlit polar cap compared to the winter hemisphere. *Wang et al.* [2005] also reported that the FAC densities in the Southern Hemisphere on the dayside are generally larger during sunlit conditions than during darkness by a factor of 2. Since the ratio between summer and winter net duskward current intensity and the change in slope of the E_m dependence both have a value of about 2, it is reasonable to conclude that the seasonal variation is caused by changing conductivity. This infers that the duskward auroral currents react as driven by a voltage source, responding directly to the dayside merging electric field. Conversely, the R2 FACs may well react differently to changes of E_m.

One aspect to be noted is the clearly larger net duskward current in the Northern Hemisphere. On average, the ratio between the Northern and Southern Hemispheres amounts to 1.5 (see Figure 7). Similar values for the Northern Hemisphere dominance by 1.4 can be found when comparing the slopes between the duskward current and E_m for the respective seasons (see Table 1). As a consequence of this dominance some features of the Northern Hemisphere are also visible in the full-orbit results. An obvious example is the net current peak in Figure 3a at 15 LT around June. The same current peak can be found in the net current distribution for the Northern Hemisphere (see Figure 6, left). In addition, one can also see in Figure 4 that the net duskward current intensity from orbits around noon is larger in northern summer (June solstice) than in southern summer (December solstice). When assuming a solar wind-driven voltage source our results infer that the summer-time conductance in the Northern Hemisphere polar cap is on the order of 1.5 higher than in the Southern Hemisphere. We have compared the solar zenith angle variations over the 5 years between the two hemispheres but obtained only small mean differences on the order of 1°. Other quantities must be responsible for the hemispheric asymmetry. Most likely the ion-neutral collision frequency makes the difference causing a higher Pedersen conductance in the northern summer hemisphere. For the collision frequency also the neutral density plays a role. More dedicated studies are required for resolving the hemispheric asymmetry.

5.3. Net Antisunward Current

From dawn-dusk orbits we have estimated a net antisunward current. Such an antisunward net current was deduced first from Magsat observations [*Suzuki and Fukushima*, 1982; *Suzuki et al.*, 1985]. The amplitudes of net antisunward currents that we derived from full orbits are about 0.2 MA for E_m ranging from 1 to 2 mV/m (see Figure 3b). Similar values have been obtained by *Suzuki et al.* [1985]. The magnitude of the net antisunward current increases as E_m increases (see Figure 3 and Table 1). *Suzuki and Fukushima* [1984] reported that the intensity of antisunward currents below the Magsat orbit is well correlated with the *AE* index during magnetic storms, whereas such a space current is almost absent under quiet conditions. Similar results are reported by *Nakano et al.* [2002], who found that the net antisunward FAC intensity deduced from the east-west magnetic disturbances at midlatitude ground geomagnetic observatories is linearly correlated with the normalized *AE* index.

For the interpretation of the observed net auroral currents we would like to go a little more into details. The net antisunward currents and the net duskward currents are of quite different character. The duskward currents crossing the polar cap are expected to be Pedersen currents connecting the excessive R1 FACs on the two flanks. Their intensity is closely controlled by the conductance. Conversely, the sunward/antisunward currents are expected to be mainly Hall currents, which encircle the R1 FACs (see Figure 1) and are to first-order source-free. The three-dimensional current distribution can be expressed as

$$j_{//} = \nabla\cdot\left(\sum\nolimits_P \vec{E}_\perp - \sum\nolimits_H \frac{\vec{E}_\perp \times \vec{B}}{B}\right) \tag{7}$$

where $j_{//}$ is the field-aligned current density, Σ_P and Σ_H are height-integrated Pedersen and Hall conductances, $E_\perp$ is the horizontal electric field, and B is the ambient magnetic field. In case of a homogenous conductivity distribution only the divergence of the Pedersen current contributes to the FACs. In case of conductivity gradients equation (7) has to be expanded as

$$j_{//} = \sum\nolimits_P \nabla\cdot\vec{E}_\perp + \nabla\sum\nolimits_P\cdot\vec{E}_\perp - \nabla\sum\nolimits_H\cdot\frac{\vec{E}_\perp\times\vec{B}}{B} - \sum\nolimits_H \nabla\cdot\frac{\vec{E}_\perp\times\vec{B}}{B} \tag{8}$$

The last term in equation (8) is again source-free and vanishes therefore. But within regions of conductivity gradients the Hall current also contributes to the FACs.

From the distribution of sunlit areas at polar region it can be expected that the location and intensity of conductivity gradients highly depend on season. Our observations confirm that the net antisunward current derived at high latitude in the two hemispheres shows a clear seasonal variation. Different from the net duskward current, the net antisunward current exhibits larger values in local winter than in local summer (see Figures 7b and 7d). The ratio of the amplitudes between summer and winter is 0.73 in the Northern Hemisphere and 0.67 in the Southern Hemisphere. From Table 1 one can see that the obtained slopes representing the dependence of the net antisunward current on E_m also confirm this seasonal dependence. During local summer the whole polar region is sunlit, and conductivity gradients are expected to be small. During winter the whole region is in darkness, and precipitating electrons are mainly responsible for enhancing the conductivity along the auroral oval. This leads to the fact that the antisunward auroral electrojets are only partly closed by the sunward current over the polar cap, due to the low polar cap conductivity in winter. The steep conductivity gradient from the auroral oval to the dark polar cap on the nightside causes that a good part of the Hall current is diverted into upward FACs at the poleward boundary of the auroral oval. This imbalance in antisunward to sunward Hall current can be detected as net current on dawn-dusk orbits. *Wang et al.* [2010] reported, based on physical modeling and Defense Meteorological Satellite Program observations, that the seasonal variation of the Pedersen conductivity latitudinal gradient maximizes in winter and minimizes in summer (see their Figure 7), exhibiting an average ratio between summer and winter of about 0.6. Even though they did not address the seasonal variation of Hall conductivity gradients, we can assume a similar ratio since the two conductances vary in similar ways.

The seasonal dependence of the unclosed antisunward current has also been studied by *Nakano et al.* [2002]. According to their approach (see their Figure 7) the net antisunward current intensity depends on the

difference between the total auroral electrojet current and the sunward return current across the polar cap. They conclude that the net current is smaller in summer than in winter because of the difference in seasonal variation of conductivity in the auroral oval and the polar cap. However, they offer no ratio of antisunward net current between summer and winter.

We have found stronger net duskward currents in the Northern Hemisphere than in the Southern Hemisphere. This has been attributed to a higher conductivity in the polar cap region. Conversely, we observed weaker net antisunward currents in the Northern Hemisphere than in the Southern Hemisphere. This is consistent with a smaller conductivity gradient from the auroral oval to the polar cap in the Northern Hemisphere. During the respective summer seasons the net antisunward currents are comparable in the two hemispheres, but for winter conditions they are stronger by about 7% in the Southern Hemisphere (see Figures 7b and 7d).

Suzuki and Fukushima [1984] suggested that the partial diversion of antisunward currents (electrojets) into FACs is responsible for the development of an asymmetric ring current in the magnetosphere during magnetic storms. This is an interesting concept, but it would need to be confirmed observationally. Already years before the first report of antisunward net current observations *Crooker and Siscoe* [1981] discussed the presence and cause for these currents. Their description of the antisunward current is identical with ours given in equation (8). When integrating the third term along the dawn/dusk orbit, the same value results as that given by equation (4) of *Crooker and Siscoe* [1981]. Physically, they argue that the R2 FAC ring is rotated westward during times of magnetic activity, resulting in gaps for current closure and excessive downward R1 FACs around noon and enhanced upward R1 FACs in the midnight sector. Interestingly, they argue that the enhanced low-latitude magnetic field effect in the evening sector during magnetic storms is not caused by feeding the antisunward net currents through the partial ring current. But they claim that the asymmetric *Dst* effect during the storm main phase is just a consequence of the magnetic field generated by the current loop including the FACs at noon and midnight and the related antisunward current closure. Our observations show that the amount of net antisunward current differs considerably between the hemispheres and this difference varies with season. These variations may help to distinguish between the different models for asymmetric *Dst* effect. More investigations are needed for characterizing the actual three-dimensional current system during magnetically active periods.

6. Summary

By applying Ampère's integral law to the along-track component of magnetic field readings from the CHAMP satellite, the net ionospheric currents are deduced and their characteristics are systematically investigated. For the first time a full local time and seasonal distribution has been derived. The main findings of the present study are summarized as follows:

1. It is found that the intensities and directions of the net currents vary with orbit local time. The net currents derived from noon-midnight orbits are directed duskward, and antisunward currents are deduced from dawn-dusk orbits. On average, the intensity of the net duskward current is about 2 times larger than that of the antisunward current, reaching maximum net duskward (antisunward) currents of about 2 (1) MA when the merging electric field (E_m) exceeds 4 mV/m.
2. The amplitudes of the net currents become stronger when the solar wind input is enhanced, exhibiting a good linear relation between net current intensities and E_m values. The slopes of net current versus E_m differ between the hemispheres and vary with orbit local time and season.
3. Seasonal variations of net current intensity are small for full orbit estimates. This implies a good compensation of seasonal effects between the hemispheres. Conversely, hemispheric results show prominent differences between local summer and winter current intensities.
4. For the hemispheric net duskward current, which is assumed to represent the cross-polar cap Pedersen current driven by excessive R1 FACs, the intensity is twice as large in summer than in winter. We relate the seasonal variation of the net duskward current to conductivity changes. The summer-time duskward currents are larger by a factor of 1.5 in the Northern Hemisphere than in the Southern Hemisphere.
5. The hemispheric net antisunward currents show an opposite seasonal variation; largest values are observed during winter season. The ratio of summer to winter amounts to about 0.7 in both hemispheres. We relate these currents mainly to Hall currents not closed in the ionosphere. In the presence of

conductivity gradients part of the Hall current is diverted out of the ionosphere by FACs, resulting in net antisunward currents. Conductivity gradients between auroral oval and polar cap are larger in winter than in summer.

An issue that should be addressed in later studies is how the diverted Hall currents are closed in the magnetosphere. The traditional opinion of current routing through the partial ring current may not be the last word.

Acknowledgments
The CHAMP mission was sponsored by the Space Agency of the German Aerospace Center (DLR) through funds of the Federal Ministry of Economics and Technology. The CHAMP magnetic field data (product identifier: CH-ME-3-MAG) are available at ftp://magftp.gfz-potsdam.de/CHAMP/L3_DATA. The OMNI data are available at ftp://spdf.gsfc.nasa.gov/pub/data/omni/high_res_omni/. The work of Yun-Liang Zhou is supported by the National Nature Science Foundation of China (41274194 and 41431073) and the China Scholarship Council (201506275011).

References

Christiansen, F., V. O. Papitashvili, and T. Neubert (2002), Seasonal variations of high-latitude field-aligned currents inferred from Ørsted and Magsat observations, *J. Geophys. Res.*, *107*(A2), 1029, doi:10.1029/2001JA900104.

Cowley, S. W. H. (2000), Magnetosphere-ionosphere interactions: A tutorial review, in *Magnetospheric Current Systems*, *Geophys. Monogr. Ser.*, vol. 118, edited by S. Ohtani et al., pp. 91–106, AGU, Washington, D. C., doi:10.1029/GM118p0091.

Crooker, N. O., and G. L. Siscoe (1981), Birkeland currents as the cause of the low-latitude asymmetric disturbance field, *J. Geophys. Res.*, *86*, 11,201–11,210, doi:10.1029/JA086iA13p11201.

Fujii, R., T. Iijima, T. A. Potemra, and M. Sugiura (1981), Seasonal dependence of large-scale Birkeland currents, *Geophys. Res. Lett.*, *8*, 1103–1106, doi:10.1029/GL008i010p01103.

Fukushima, N. (1976), Generalized theorem for no ground magnetic effect of vertical currents connected with Pedersen currents in the uniform-conductivity ionosphere, *Rep. Ionos. Space Res. Japan*, *30*, 35–40.

Iijima, T., and T. Potemra (1976), Field-aligned currents in the dayside cusp observed by triad, *J. Geophys. Res.*, *81*, 5971–5979, doi:10.1029/JA081i034p05971.

Kervalishvili, G. N., and H. Lühr (2014), Climatology of zonal wind and large-scale FAC with respect to the density anomaly in the cusp region: Seasonal, solar cycle, and IMF By dependence, *Ann. Geophys.*, *32*, 249–261, doi:10.5194/angeo-32-249-2014.

Lühr, H., and S. Maus (2010), Solar cycle dependence of quiet-time magnetospheric currents and a model of their near-Earth magnetic fields, *Earth Planets Space*, *62*, 843–848, doi:10.5047/eps.2010.07.012.

Maus, S., C. Manoj, J. Rauberg, I. Michaelis, M. Rother, and H. Lühr (2010), NOAA/NGDC candidate models for the 11th generation International Geomagnetic Reference Field and the concurrent release of the 6th generation Potsdam Magnetic Model of the Earth, *Earth Planets Space*, *62*, 729–735, doi:10.5047/eps.2010.07.006.

Nakano, S., T. Iyemori, and S. Yamashita (2002), Net field-aligned currents controlled by the polar ionospheric conductivity, *J. Geophys. Res.*, *107*(A5), 1056, doi:10.1029/2001JA900177.

Newell, P. T., T. Sotirelis, K. Liou, C.-I. Meng, and F. J. Rich (2007), A nearly universal solar wind-magnetosphere coupling function inferred from 10 magnetospheric state variables, *J. Geophys. Res.*, *112*, A01206, doi:10.1029/2006JA012015.

Reigber, C., H. Lühr, and P. Schwintzer (2002), CHAMP mission status, *Adv. Space Res.*, *30*, 129–134, doi:10.1016/S0273-1177(02)00276-4.

Russell, C. T., and R. L. McPherron (1973), Semiannual variation of geomagnetic activity, *J. Geophys. Res.*, *78*, 92–108, doi:10.1029/JA078i001p00092.

Stauning, P., and F. Primdahl (2000), First detection of global dawn-dusk ionospheric current intensities using Ampère's integral law on Ørsted orbits, *Geophys. Res. Lett.*, *27*, 3273–3276, doi:10.1029/2000GL011954.

Suzuki, A., and N. Fukushima (1982), Sunward or anti-sunward electric current in space below the MAGSAT level, *Geophys. Res. Lett.*, *9*, 345–347, doi:10.1029/GL009i004p00345.

Suzuki, A., and N. Fukushima (1984), Anti-sunward current below the MAGSAT level during magnetic storms, *J. Geomagn. Geoelectr.*, *36*, 493–506, doi:10.5636/jgg.36.493.

Suzuki, A., M. Yanagisawa, and N. Fukushima (1985), Anti-sunward space currents below the MAGSAT level during magnetic storms and its possible connection with partial ring current in the magnetosphere, *J. Geophys. Res.*, *90*, 2465–2471, doi:10.1029/JB090iB03p02465.

Wang, H., H. Lühr, and S. Y. Ma (2005), Solar zenith angle and merging electric field control of field-aligned currents: A statistical study of the Southern Hemisphere, *J. Geophys. Res.*, *110*, A03306, doi:10.1029/2004JA010530.

Wang, H., H. Lühr, and A. J. Ridley (2010), Plasma convection jets near the poleward boundary of the nightside auroral oval and their relation to Pedersen conductivity gradients, *Ann. Geophys.*, *28*(4), 969–976, doi:10.5194/angeo-28-969-2010.